Imaging Carbon Nanotube Interactions, Diffusion, and Stability in Nanopores

Shannon L. Eichmann,[†] Billy Smith,[‡] Gulsum Meric,[†] D. Howard Fairbrother,[‡] and Michael A. Bevan[†,*]

[†]Department of Chemical and Biomolecular Engineering, [‡]Department of Chemistry, Johns Hopkins University, Baltimore, Maryland 21218, United States

ABSTRACT We report optical microscopy measurements of three-dimensional trajectories of individual multiwalled carbon nanotubes (MWCNTs) in nanoscale silica slit pores. Trajectories are analyzed to nonintrusively measure MWCNT interactions, diffusion, and stability as a function of pH and ionic strength. Evanescent wave scattering is used to track MWCNT positions normal to pore walls with nanometer-scale resolution, and video microscopy is used to track lateral positions with spatial resolution comparable to the diffraction limit. Analysis of MWCNT excursions normal to pore walls yields particle–wall potentials that agree with theoretical electrostatic and van der Waals potentials assuming a rotationally averaged potential of mean force. MWCNT lateral mean square displacements are used to quantify translational diffusivities, which are comparable to predictions based on the best available theories. Finally, measured MWCNT pH and ionic strength dependent stabilities are in excellent agreement with predictions. Our findings demonstrate novel measurement and modeling tools to understand the behavior of confined MWCNTs relevant to a broad range of applications.

KEYWORDS: multiwalled carbon nanotubes · video microscopy · evanescent wave scattering · interaction potentials · confined diffusion · single-particle measurements

Carbon nanotubes (CNTs) have unique physical and chemical properties that make them promising for advancing and enabling a broad range of existing and emerging applications. At various stages during their synthesis, processing, and use in applications, their interactions with surfaces and in confined environments determine their transport properties and whether they become reversibly or irreversibly deposited. For example, CNT transport and deposition on surfaces and in confined geometries is important in material and device fabrication,[1] *in vivo* drug delivery or imaging applications,[2] and their transport and fate in the environment.[3] As a result, the ability to measure CNT interactions and transport in interfacial and confined geometries provides fundamental information that can be used to interpret and predict their behavior in a broad range of technologies.

While numerous analytical techniques are available to characterize CNT physicochemical properties,[4] relatively few methods are available to directly measure interactions between CNTs and surfaces on scales relevant to transport and stability. For example, atomic force microscopy (AFM) is one approach capable of measuring CNT interactions. A nonexhaustive review of some relevant examples using AFM to probe CNT interactions includes measurements of CNTs interacting with surfaces in water,[5] polymers in air,[6] alkane thiol-modified gold surfaces,[7] and different chemical moieties.[8] However, the mechanical nature of AFM measurements limits their resolution to >piconewton forces and energies ≫the thermal energy, kT. This is important because kT is the inherent energy scale of Brownian motion, and consequently the magnitude of interactions relative to kT determines whether particles diffuse (with only hydrodynamic hindrance), intermittently deposit and diffuse, or deposit irreversibly on surfaces. Although AFM measurements of CNT–surface interactions are "direct", their mechanically intrusive nature limits their applicability to understanding CNT diffusion and deposition on surfaces in the absence of strong external forces.

Likewise, few methods are available to directly measure transport of individual CNTs near surfaces and in confinement. Fluorescence imaging is one approach that has been used to image single-walled CNTs (SWCNTs) in confinement. Examples of such measurements include studies of fluorescently labeled SWCNT rotation, translation, and bending dynamics,[9] which have also been performed using unlabeled SWCNTs using their intrinsic near-infrared fluorescence.[10,11] This approach has recently been adapted to image SWCNT Brownian motion in a macromolecular gel matrix medium,[12] where translational and rotational diffusion were captured by reptation[13] models. While these studies measure mechanisms of SWCNT transport with connections to their mechanical properties, they do not capture the

* Address correspondence to mabevan@jhu.edu.

Received for review May 10, 2011 and accepted June 7, 2011.

Published online June 07, 2011
10.1021/nn2017149

additional roles that conservative (*e.g.*, electrostatic, van der Waals) and dissipative (*e.g.*, hydrodynamic) forces between CNTs and rigid surfaces contribute in determining CNT transport or deposition.

In terms of the precedent for measuring interactions and dynamics of confined nanoparticles other than CNTs, we briefly summarize our recent measurements of direct relevance to this paper. In previous papers,[14,15] we measured three-dimensional trajectories of 50−250 nm Au spherical nanoparticles in slit pores using integrated evanescent wave (EW) and video microscopy (VM) methods that we originally developed for micrometer-sized colloids.[16,17] For low ionic strength aqueous media, Au nanoparticle interactions with confining surfaces were well described by DLVO electrostatic potentials.[14] However, in these same measurements, translational diffusivities were lower than expected based on predicted hydrodynamic interactions with the confining surfaces. This discrepancy was attributed to an additional electroviscous dissipation associated with thick and strongly overlapping electrostatic double layers.[18] For protein-stabilized Au nanoparticles in high ionic strength physiological media, macromolecular and van der Waals interactions and translational diffusion were all well described by existing theoretical models.[15] The success of these measurements and predictions provide a basis to move onto the more complex case of confined anisotropic CNTs.

In this work, we adapt and extend the experimental methods and analyses used for spherical Au nanoparticles to study the interactions, diffusion, and stability of CNTs in nanoscale slit pores. In particular, we report the use of EW and VM to measure real-space, real-time 3D subdiffraction-limit-sized multiwalled CNT (MWCNT) trajectories confined between glass microscope slides separated by 300 nm (see Figure 1). Dispersed MWCNTs were created by direct covalent attachment of oxygen-containing functional groups onto the sidewalls.[19] Statistical mechanical and dynamic analyses[20] of these trajectories are used in a self-consistent fashion to obtain potentials of mean force and translational diffusivities that we compare with theoretical predictions. Information obtained in these analyses is used to predict CNT stability as a function of solution ionic strength and pH dependent surface charge, in excellent agreement with direct measurements. These results demonstrate direct, label-free, nonintrusive measurements of CNT interactions in nanopores on the *kT* and nanometer scales for time scales spanning milliseconds to hours. These measurements and associated analysis provide fundamental information to interpret and predict CNT transport and stability as a function of solution medium and surface chemistries that are likely to be encountered in a variety of processing and application environments.

THEORY

Potential Energy Profiles. MWCNT interactions in this work are considered to be averaged over all rotational degrees of freedom so that they can be treated using spherical potentials of mean force. Steric interactions are not considered in the net potential in this work since oligomeric or macromolecular surfactants were not employed for MWCNT stabilization.

Based on these assumptions, we compute the net MWCNT potential energy profile as the sum of surface forces acting on a spherical nanoparticle confined between charged parallel planar surfaces as

$$u(z) = u_{\mathrm{E,\,LW}}(z) + u_{\mathrm{E,\,UW}}(\delta - z) + u_{\mathrm{vdW,\,LW}}(z) + u_{\mathrm{vdW,\,UW}}(\delta - z) \quad (1)$$

where z is the bottom wall surface-to-nanoparticle center separation, δ is the distance between the parallel planar pore wall surfaces, $\delta - z$ is the upper wall surface-to-nanoparticle center separation, and the subscripts "LW" and "UW" refer to the lower and upper walls. Other important length scales include the effective spherical nanoparticle radius, a, and the effective bottom wall surface-to-nanoparticle surface separation, $h = z - a$.

For thick double layers ($\kappa a \approx 1$) that experience significant overlap ($\kappa h \approx 1$),[21] the electrostatic potential, $u_{\mathrm{E}}(z)$, is given as[22]

$$u_{\mathrm{E}}(z) = 4\pi\varepsilon a \psi_{\mathrm{P}} \psi_{\mathrm{W}} \exp[-\kappa(z - a)] \quad (2)$$

where a is the nanoparticle radius, ε is the dielectric permittivity of water, κ^{-1} is the Debye length, and ψ_{P} and ψ_{W} are the Stern potentials of the particle and the wall. The Stern potentials can be obtained by either equating them with the ζ potential obtained from electrophoretic mobility, v, measurements using the Smoluchowski equation,

$$\psi_{\mathrm{SM}} = \zeta = (\mu/\varepsilon)v \quad (3)$$

where μ is the continuous medium viscosity, or relating them to surface charge density, σ, measurements using the Guoy−Chapman equation,

$$\psi_{\mathrm{GC}} = (2kT/e)\sinh^{-1}\left(\frac{\sigma e}{2kT\varepsilon\kappa}\right) \quad (4)$$

The van der Waals interaction potential, $u_{\mathrm{vdW}}(z)$, is given by[23]

$$u_{\mathrm{vdW}}(z) = \frac{A}{6}\left[\frac{2a}{(z-a)}\left(\frac{z}{z+a}\right) - \ln\left(\frac{z+a}{z-a}\right)\right] \quad (5)$$

where A is the Hamaker constant.

The net potential energy profile in eq 1 is related to the distribution of heights sampled within the gap between parallel walls, $p(z)$, given by Boltzmann's equation as

$$p(z) = p_{\mathrm{n}} \exp[-u(z)/kT] \quad (6)$$

where p_{n} is a normalization constant related to the number of height observations,[16,17] k is Boltzmann's

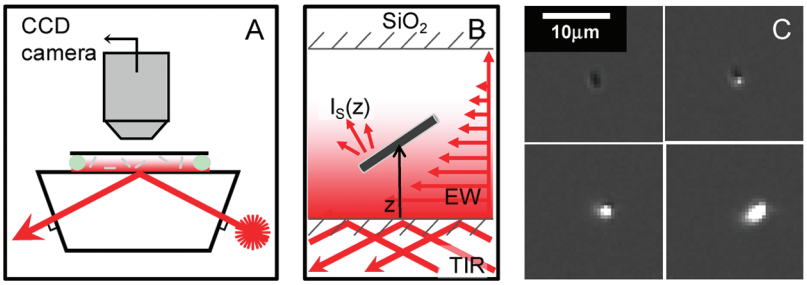

Figure 1. Schematics and images of experimental setup and confined MWCNT scattering in an evanescent wave. (A) Schematic of digital video optical microscopy setup to monitor scattering from single MWCNTs confined between coverslips separated by ~320 nm silica colloid spacers. (B) Illustration of elevation-dependent scattering of MWCNT in exponentially decaying evanescent wave (EW) formed by total internal reflection (TIR) at SiO_2/water interface. (C) CCD camera images of elevation- and orientation-dependent scattering of an individual MWCNT with a length greater than the optical diffraction limit.

constant, and T is the absolute temperature. Equation 6 can be inverted to obtain the interaction potential from a measured height histogram as

$$\frac{u(z) - u(z_m)}{kT} = \ln\left[\frac{p(z_m)}{p(z)}\right] \quad (7)$$

where z_m is the most probable height.

Confined Lateral Diffusion. The translational diffusion coefficient of a spherical nanoparticle far from any other particles or boundaries is given as[21]

$$D_0 = kT/6\pi\mu a \quad (8)$$

For a single spherical nanoparticle confined between two parallel planar surfaces, the hydrodynamic hindrance to lateral diffusion can be accounted for at any given elevation with the gap using

$$D_{\parallel}(z, a, \delta) = D_0 f_{\parallel}(z, a, \delta) \quad (9)$$

where analytical solutions are available for $f_{\parallel}(z,a,\delta)$.[24,25] The average lateral diffusion coefficient, $\langle D_{\parallel}\rangle$, can be obtained as an average over the equilibrium height distribution (eq 6) as given by[26]

$$\langle D_{\parallel}\rangle = \frac{\int D_{\parallel}(z, a, \delta)\, p(z)\, dz}{\int p(z)\, dz} \quad (10)$$

For comparison, the translational diffusion coefficient of a rod-shaped nanoparticle far from any other particles or boundaries is given as[27,28]

$$D_{T,\,Rod} = \frac{kT}{3\pi\mu L}(\ln(\gamma) + 0.312 + 0.565\gamma^{-1} - 0.100\gamma^{-2}) \quad (11)$$

where L is the rod length, d is the rod diameter, and $\gamma = L/d$.

Stability Ratio. The stability ratio, W, which is the reciprocal of the rate of rapid deposition compared to the deposition rate in the presence of electrostatic energy barriers, can be predicted using Fuchs's theory[29] with hydrodynamic interactions[30,31] as given by[21]

$$W = 2a\int_0^{\infty} [D_0/D_{\perp}(z)]\exp[u(z)](z - a)^{-2}\, dz \quad (12)$$

where the hydrodynamic hindrance to diffusion normal to the confining walls is given by

$$D_{\perp}(z, a, \delta) = D_0 f_{\perp}(z, a, \delta) \quad (13)$$

where analytical solutions are available for $f_{\perp}(z,a,\delta)$.[26,32]

RESULTS AND DISCUSSION

Experimental Configuration. Figure 1 provides a schematic depiction of the experimental configuration for EW and VM imaging of oxidized MWCNTs confined between parallel glass (silica) coverslips separated by several hundred nanometers. Figure 1A shows the apparatus (not to scale) including an upright microscope with a CCD camera for digital imaging and analysis and a small batch cell optically coupled to a dovetail prism for generating the EW *via* total internal reflection of a laser. The cell is oriented and leveled so that the direction of gravity is normal to and toward the bottom slide. However, gravity has minimal influence on the measurements in this work given the negligible buoyant weight of the MWCNTs *via* their low density and small dimensions.

Figure 1B shows a magnified schematic (approximately to scale) of a MWCNT with arbitrary orientation scattering the EW within the slit pore. The slit pore gap was fixed to a known value by the addition of monodisperse 320 nm silica colloidal spacers. These were added at a sufficiently low concentration so that imaging of MWCNTs could be performed without any spacers being present or scattering within a given imaging window. The EW illuminates a patch within the cell with lateral dimensions comparable to the 1 mm laser beam diameter. The EW penetration depth of β^{-1} = 113 nm ($3\beta^{-1}$ = 339 nm) essentially illuminates the entire depth of the 320 nm slit pore. No significant increase in background was observed from EW scattering from the top microscope slide. Complete EW illumination of the slit pore allows for continuous monitoring of MWCNT trajectories normal to the confining silica surfaces with nanometer resolution[33] and lateral diffusion within half a pixel (*i.e.*, ~300−600 nm in the present work).

Figure 1C shows representative static images obtained from a movie (included in the Supporting Information) of a relatively large MWCNT with transmitted light illumination in addition to EW scattering. This particular MWCNT has a length greater than the optical diffraction limit, which allows its orientation to be visible from the both the transmitted light image as well as the anisotropic EW scattering pattern. The greatest scattering is observed when the orientation and elevation of the MWCNT cause it to encounter the greatest EW intensity near the bottom surface (*e.g.*, Figure 1C lower, right panel). The least scattering is observed for positions near the top confining surface (*e.g.*, Figure 1C top, left panel).

While the images in Figure 1C demonstrate the ability to dynamically image MWCNTs with at least one dimension greater than the optical diffraction limit, the remainder of this paper measures MWCNTs with all dimensions below the diffraction limit. The significant optical contrast[34] of MWCNTs compared to the aqueous medium produces sufficient EW scattering intensity, despite their small size, to allow for quantitative tracking measurements using a standard CCD camera and optics. The subdiffraction limit dimensions of the MWCNTs measured in this study are evident because EW illumination shows only isotropic patterns that are not characteristic of rod shapes (scattering anisotropy could not be detected within the spatiotemporal resolution of our CCD camera and using a randomly polarized HeNe laser). This suggests that all MWCNT dimensions are <200 nm (*i.e.*, a standard estimate of the optical diffraction limit for visible wavelengths). The Supporting Information includes a movie of several subdiffraction limit sized MWCNTs displaying isotropic scattering in contrast to the anisotropic scattering of the superdiffraction limit sized MWCNT shown in Figure 1C.

Because we select only small-length rods ($L \approx$ 200 nm), their EW scattering signal is isotropic and they should be able to rotate within the slit pores (*i.e.*, they do not physically touch the pore walls although orientation-dependent hydrodynamic interactions can influence their diffusion). Based on this information, as a first approximation, we analyze their scattering and physical interactions based on models for spherical nanoparticles in slit pores.[14,15] Theories for rod−wall interactions are available,[35−37] but the authors are not aware of a theory for EW scattering of rods at arbitrary orientations. We use theories for spherical nanoparticles by considering MWCNT potentials of mean force to be averaged over all orientations and as effective sphere−wall interactions. For interpretation of their scattering, we apply similar reasoning in that different orientations sampled by rotational diffusion are averaged in the scattering signal obtained during the CCD camera exposure time.[15] Despite the lack of exact theories for rod-shaped particle−wall interactions or EW scattering, we believe the internal consistency of our findings in the final analysis justifies our approach as an important first step, even in the presence of some uncertainties. As a result, we proceed by interpreting MWCNT scattering and measurements using sphere models and discuss their appropriateness later in the context of our results.

Independent MWCNT Characterization. To aid the interpretation of our microscopy measurements, we performed independent characterization of the MWCNTs prior to any size fractionation as part of our microscopy measurements. Figure 2A and B include AFM characterization of rod lengths with a representative raw image and length distribution histogram. This shows some rods are as long as 5 μm, but most are ~200 nm. Because the persistence length of MWCNTs is on the order of $L_P \approx 300$ nm,[38] MWCNTs with lengths of $L <$ 300 nm can be considered as essentially rigid. As already mentioned, rods with lengths greater than the optical diffraction limit can be identified from their anisotropic scattering pattern and are not included in our analysis. Figure 2C shows a representative TEM cross-sectional image of a MWCNT that indicates a rod diameter of ~15 nm. Dynamic light scattering (DLS) measurements performed on the MWCNTs used in the present study yielded translational diffusion coefficients that correspond to spherical particles with hydrodynamic diameters of $2a = 43-1340$ nm (eq 8). For rods with 15 nm cross sections, these hydrodynamic diameters correspond to lengths of $L = 100-10340$ nm (eq 11). The rod lengths inferred from DLS are consistent with the AFM measurements when considering the flexibility of MWCNTs with $L > L_P$ as well as their greater statistical sampling and size-dependent intensity contributions in DLS measurements.

Figure 2D shows properties related to the pH-dependent MWCNT surface charge and surface potential for use in models of electrostatic interactions between MWCNTs and silica surfaces. The solid line is the pH-dependent surface potential for silica.[39,40] Using published results for MWCNTs prepared in a manner similar to the ones used here,[19] Figure 2D shows pH-dependent zeta potentials (circles) computed from measured mobilities using the Smoluchowski equation (eq 3) and Stern potentials (dashed line) computed from measured surface charge densities using the Guoy−Chapman equation (eq 4). The zeta and Stern potentials are equivalent if ~10% of surface charge groups are dissociated on the MWCNTs (*i.e.*, ~90% of counterions are bound in a dynamic equilibrium with the charged surface). For oxidized MWCNTs, surface charge arises predominantly as a result of carboxylic acid group deprotonation. From these previous results, we predict a surface potential of −40 mV at pH = 6 for the 7.9% oxygen MWCNTs used in this study, which is in excellent agreement with the zeta potential measured in this work at

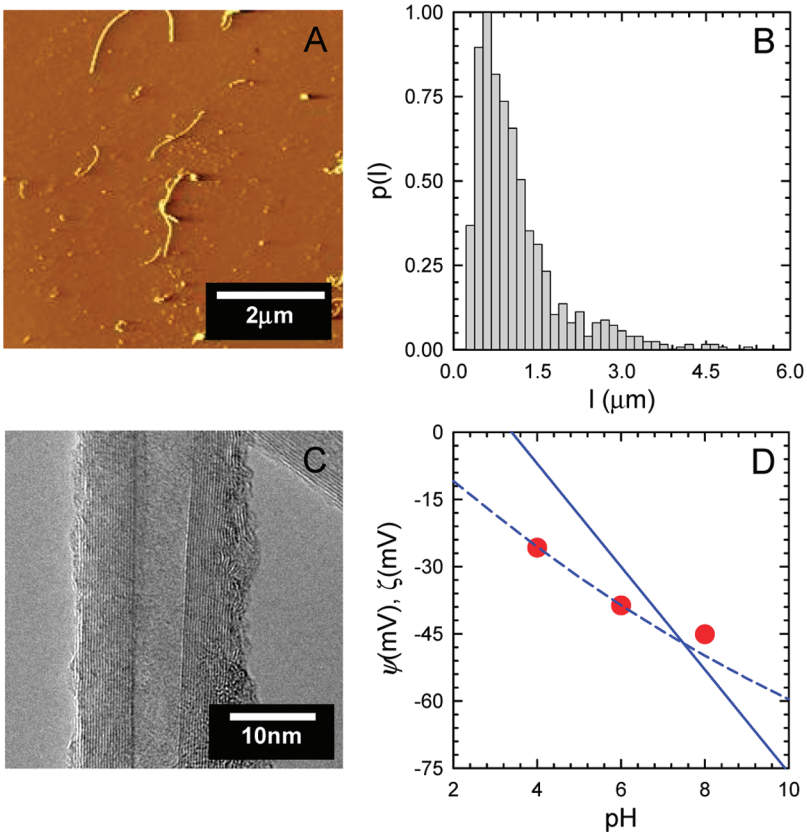

Figure 2. Independent characterization of oxidized MWCNT physical and surface charge properties. (A) Representative AFM image of MWCNTs dried on a TEM grid used to measure the MWCNT length distribution. (B) MWCNT length distribution from AFM measurements. (C) Representative high-resolution TEM image of MWCNT cross section showing ~15 nm diameter. (D) Stern (dashed line) and zeta (circles) potentials for MWCNTs inferred from previous electrophoretic mobility and potentiometric titration measurements[19] using the Guoy–Chapman (eq 4) and Smoluchowski (eq 3) equations. The solid line is the pH-dependent surface potential for silica.[39,40]

pH = 6. As a result, we use the pH-dependent Stern potential in Figure 2D when analyzing electrostatic interactions.

Potential Energy Profiles *vs* pH and Ionic Strength. Using the MWCNTs characterized in Figure 2, we now proceed with measurements and analysis of MWCNT–silica wall interactions using the experimental configuration described in Figure 1. We measure and interpret MWCNT–silica wall interactions using the methods and analyses we previously developed for Au nanoparticle–silica interactions in slit pores.[14,15] As already noted, we use these methods without modification and then discuss their appropriateness for MWCNTs in the context of our results. We begin by measuring time-averaged potential energy profiles (energy *vs* separation) between MWCNTs and confining silica pore wall surfaces that arise from superposition of electrostatic and van der Waals forces. When electrostatic repulsion between the negatively charged MWCNTs and negatively charged silica surfaces dominates, MWCNTs experience Brownian excursions around the mechanical equilibrium position in the middle of the slit pore. When van der Waals attraction dominates, MWCNTs deposit irreversibly on the top or bottom surfaces. While van der Waals attraction depends weakly on solution ionic strength,[37] the dominant factors influencing the net MWCNT–silica interaction are related to how solution chemistry (*i.e.*, ionic strength, pH) and surface chemistry (*i.e.*, charge density, dissociation) increase or decrease electrostatic repulsion.

In Figure 3, we use EW and VM to make a first attempt to directly quantify MWCNT–silica potential energy *vs* separation profiles, which to the authors' knowledge has not been previously attempted using any method. Figure 3A and B show theoretical predictions and EW/VM measurements *vs* pH = 3, 6, and 9 with no added NaCl, and Figure 3C and D show predictions and measurements *vs* [NaCl] = 0, 1, and 10 mM at pH = 6. The predicted potentials in Figure 3A and C are shown on a separation scale relative to contact with the bottom silica surface ($z = 0$), and the measured potentials are reported on a scale, $z-z_m$, relative to the most probable height, z_m. The predicted and fit potentials are based on the parameters reported in Table 1, which denotes whether parameters were measured independently or obtained from the literature.

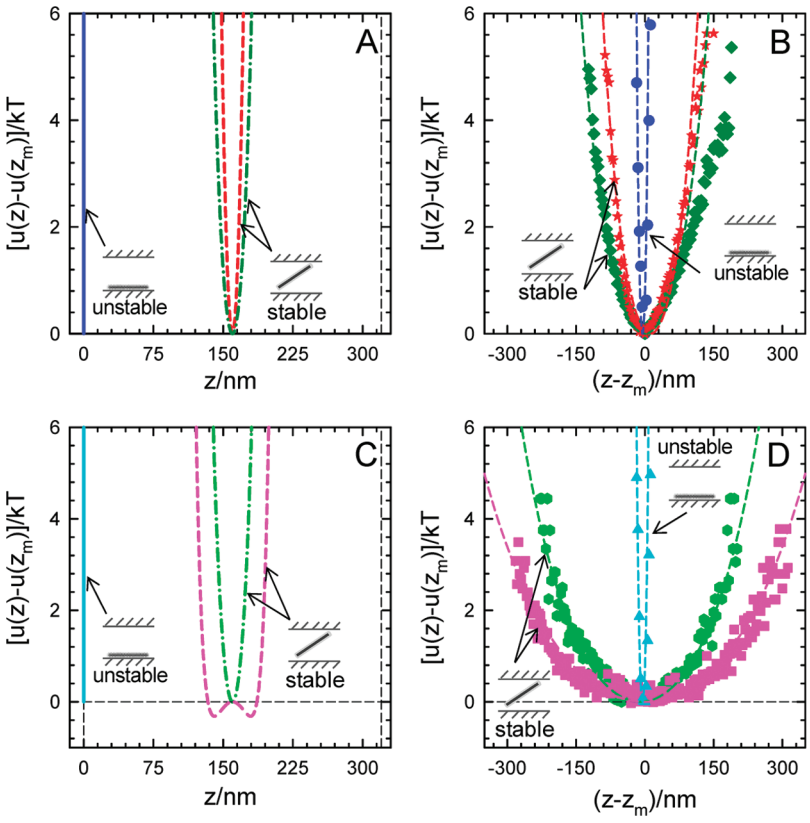

Figure 3. Predicted and measured potential energy profiles for MWCNTs interacting with parallel, confining glass (silica) microscope coverlsips separated by 320 nm SiO_2 colloids. (A) Predicted potentials using eq 1 for 200 nm spherical nanoparticles with a fixed [NaCl] = 0 mM and pH = 3 (solid blue line), 6 (dash−dot green line), and 9 (dashed red line). The separation scale is relative to the bottom microscope slide surface, and the energy scale is relative to the value at the most probable separation, z_m. (B) Measured potentials for the same conditions and color scale as (A) with symbols showing pH = 3 (circles), 6 (diamonds), and 9 (stars). The separation scale is relative to z_m. Dashed curves are predicted potentials in (A) convoluted with Gaussian kernel with standard deviations in Table 1. (C) Predicted potentials using eq 1 for 200 nm spherical nanoparticles with a fixed pH = 6 and [NaCl] = 0 mM (dash−dot green line), 1 mM (dashed pink line), and 10 mM (solid cyan line) with the same scales as (A). (D) Measured potentials for same conditions and color scale as (C) with symbols showing [NaCl] = 0 mM (hexagons), 1 mM (squares), and 10 mM (triangles) and the same scales as (B).

To obtain fits in agreement with the measured potentials, theoretical potentials were smoothed with a Gaussian convolution integral. This smoothing procedure is used to account for uncertainty in MWCNT elevations within the slit pore that result from intensity variations due to different orientations sampled by rotational diffusion at each elevation (which is not encountered for isotropic spheres). To perform smoothing, potentials were converted to height histograms *via* Boltzmann's equation (*i.e.*, eq 6), convoluted with a Gaussian kernel, and then converted back to potentials *via* inversion with Boltzmann's equation (*i.e.*, eq 7). The standard deviations of the Gaussian kernels, σ, are the only fitting parameter and are reported in Table 1.

While the Gaussian smoothing parameters cannot be compared with independent quantitative predictions (because they do not exist), the resulting potentials and smoothing parameters coincide with known limiting cases and display trends in agreement with expectations. For example, MWCNTs irreversibly deposited on the silica walls at pH = 3, [NaCl] = 0 and pH = 6, [NaCl] = 10 mM have σ = 4 nm. These small widths in the profiles of deposited particles are due to fluctuations in the lasers, detectors, apparatus, *etc.*, rather than any real excursions due to Brownian translation or rotation. The signal-to-noise ratio in these MWCNT measurements is slightly higher than experiments involving micrometer-sized spheres, which makes the deposited MWCNT profiles slightly wider. In other words, irreversibly deposited particles should have a delta function for their height distribution; consequently, any apparent fluctuations in the absence of Brownian motion provide one way to characterize the spatial resolution limit in EW scattering measurements.

The remainder of the potentials display a trend of increasing σ values for increasing widths of predicted potential energy profiles (and experimentally measured height excursions). This is consistent with MWCNTs sampling a greater range of elevations and orientations as electrostatic repulsion is diminished within the slit pores. Conversely, increasing electrostatic repulsion causes the MWCNTs to sample fewer

TABLE 1. Parameters for Theoretical Potential Energy Profiles in Figures 3–5

	1	2	3	4	5	6
$2a$/nm[a]	200	200	200	200	200	200
[NaCl]/mM[b]	0	1	10	0	0	0
pH[b]	6	6	6	3	6	9
κ^{-1}/nm[c]	13.6	7.9	3.0	9.6	13.6	13.5
δ/nm[d]	320	320	320	320	320	320
ψ_{cnt}/mV[e]	−36	−36	−36	−22	−36	−51
ψ_{sio2}/mV[e]	−30	−30	−30	5	−30	−65
A/kT[f]	28	28	28	28	28	28
$2a_{DLS}$/nm[g]	43–1348	43–1348	43–1348	43–1348	43–1348	43–1348
l_{DLS}/nm[h]	100–10340	100–10340	100–10340	100–10340	100–10340	100–10340
l_{AFM}/nm[h]	90–5810	90–5810	90–5810	90–5810	90–5810	90–5810
σ/nm[i]	84	122	4	4	45	34

[a] Effective sphere diameter (see text for explanation). [b] Prepared solution conditions. [c] Debye lengths computed from ionic strength (*i.e.*, pH and electrolyte). [d] Slit pore gap dimensions (*i.e.*, nominal spacer diameter). [e] Values obtained from literature[19,39] and shown in Figure 2D. [f] Average Hamaker constant from literature values for carbon black across water[43,44] and CNT–polystyrene across water (which should be close to CNT–silica).[45] [g] Effective hydrodynamic radius range of MWCNTs in DI water from 20 DLS measurements. [h] Effective MWCNT length DLS measured translational diffusivities. [i] Standard deviation in Gaussian convolution used to match measured and theoretical potentials in Figure 3.

orientations and elevations by confining them to the center of the slit pore, hence less smoothing. In principle, the width of the smoothing functions could be predicted by averaging the EW scattering for all MWCNT orientations and elevations with a Boltzmann weighting based on the orientation and elevation-dependent MWCNT–silica wall potential of mean force. However, although suitable expressions are available for the potential of mean force, the orientation-dependent scattering of rods in EW is not available. Future measurements and analyses will explore more rigorous approaches to predicting and interpreting these potentials.

The measured potentials appear to be consistent with the predicted potentials within the resolution of our measurements. As a result, the measurements also display the expected trends based on the ionic strength and pH dependence of electrostatic repulsion. In particular, screening electrostatic repulsion at elevated ionic strengths or reducing the MWCNT and silica surface potentials at low pHs weakens electrostatic repulsion relative to deionized water and CO_2-saturated water (*i.e.*, pH = 6). Reducing electrostatic repulsion by either mechanism first makes potential energy profiles wider by allowing MWCNTs to sample more orientations and elevations. However, further weakening electrostatic repulsion lowers the potential energy barrier, leading to irreversible deposition onto the silica pore walls by van der Waals attraction. These results demonstrate how sensitive, quantitative measurements of MWCNT interactions with silica can be related to changes in solution and surface chemistry.

Combined Effects of pH and Ionic Strength on Carbon Nanotube Diffusion. In addition to the equilibrium MWCNT–silica wall interactions in Figure 3, Figure 4 shows results characterizing MWCNT lateral dynamics within pores as a function of pH and ionic strength. Figure 4A shows the two-dimensional trajectories for conditions corresponding to (1) stable MWCNTs that exhibit unbiased 2D diffusion and (2) unstable MWCNTs that show no motion due to their irreversible deposition on one of the two microscope slide surfaces. To quantify the 2D motion parallel to the confining walls, Figure 4B shows mean squared displacements (MSDs) *vs* time using the same 3D trajectory data (and hence the same conditions) analyzed as equilibrium potential energy profiles shown in Figure 3. To clarify and emphasize this point, the integrated EW scattering and VM method used in this work (see Figure 1) allows for motion normal to the confining walls to be measured from the EW scattering signal at the same time VM tracks motion parallel to the confining walls. Indeed, to provide an internally consistent analysis, the same trajectories used to produce the potential energy profiles in Figure 3 *via* an equilibrium analysis of normal excursions are used to measure lateral diffusion in Figure 4 *via* a dynamic analysis of lateral excursions.

MWCNT translational diffusivities obtained from slopes of the MSDs *vs* time in Figure 4B display several clear trends. In the simplest case, MWCNTs display no lateral diffusion when they are deposited (*i.e.*, unstable) on one of the pore walls at low pHs and high ionic strengths. While this might appear as a trivial result since the particle–wall potentials in Figure 3 already show these particles are deposited, particles deposited on surfaces *via* normal forces should be free to move laterally in the absence of tangential forces (*i.e.*, by rolling). In practice, finite tangential forces for deposited particles (due to roughness, particle or surface deformation, lateral heterogeneity) produce barriers to lateral diffusion as observed for the deposited (unstable) MWCNTs in Figure 4. In contrast, the stable particles confined to the middle region of the slit pore are free to diffuse laterally. For stable MWCNTs, analysis

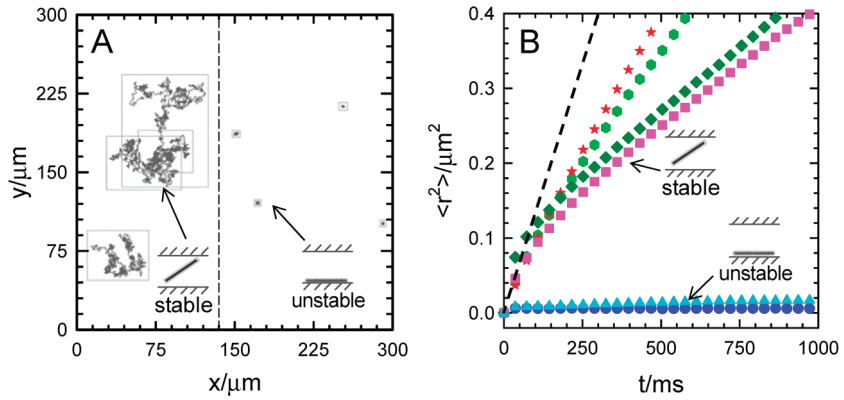

Figure 4. Lateral diffusion of MWCNTs between parallel, confining glass microscope coverslips separated by 320 nm SiO_2 colloids. (A) Two-dimensional random walk trajectories for conditions corresponding to stable MWCNTs that exhibiting unbiased 2D diffusion and unstable MWCNTs that show no motion due to irreversible deposition on one of the pore wall surfaces. (B) Mean square displacements for quasi 2D translational diffusion of MWCNTs. Conditions for each data set are as follows: pH 3/0 mM (blue circles), pH 6/10 mM (cyan triangles), pH 6/1 mM (pink squares), pH 6/0 mM (dark green diamonds), pH 6/0 mM (green hexagons), and pH 9/0 mM (red stars). Lines indicate predicted mean square displacement curves based on diffusivities from eq 10 for a 200 nm sphere in a 320 nm gap using the theoretical potentials in Figure 3.

of orthogonal 1D MSDs *vs* time did not show directional differences or parabolic upturns indicative of anistropic transport or migration due to any nonuniformities in slit pores.

To investigate whether the observed 2D translational diffusion coefficients are reasonable for stable MWCNTs, Figure 4B shows a single dashed line corresponding to a 200 nm spherical nanoparticle based on our previous measurements of Au nanoparticles.[14,15] This result includes a number of effects that influence spherical nanoparticle diffusion in slit pores. The first is the role of multibody hydrodynamic interactions that produce increasing drag (decreasing mobility) on nanoparticles for positions closer to either of the slit pores walls and produce the least drag (highest mobility) at the midplane. It should be noted that the mobility at the pore midplane is still much smaller compared to the Stokes drag on a sphere in an unbounded medium. Because the degree of hydrodynamic hindrance depends on the position normal to the wall surfaces, the average lateral diffusion coefficient is obtained as an integral average over the distribution of heights sampled by nanoparticles within the gap (*i.e.*, eq 10). This height distribution was predicted in Figure 3 in agreement with directly measured potential energy profiles and can be used in conjunction with theoretical expressions for hydrodynamic interactions to predict the lateral diffusivity of a sphere in confinement.

The dashed line also includes the role of electroviscous effects on charged nanoparticle mobilities in confinement (by multiplying the prediction in eq 10 by 0.5 as observed in Au nanoparticle measurements[14]). Electroviscous effects refer to the additional drag encountered for charged fluids moving relative to charged surfaces.[18] Electroviscous effects have an electrokinetic origin distinct from the electrostatic interactions already included in the probability distribution in eq 10. Evidence of such effects was observed in our previous measurements and modeling of ~200 nm Au nanoparticle diffusion in ~300 nm slit pores. These measurements showed that for relatively thick (*i.e.*, $\kappa_a \sim 1$) and strongly overlapping (*i.e.*, $\kappa_h \sim 1$) electrical double layers, the rate of lateral diffusion was reduced by an additional factor of 2 beyond what could be accounted for by hydrodynamic interactions alone.[14] The electrokinetic origin of this additional dissipative effect was confirmed by recovering the expected theoretical hindered diffusion coefficient in high ionic strength media where the electroviscous contribution is expected to vanish.[15]

With these effects in mind, it is clear that the stable MWCNTs in Figure 4 diffuse slower (by a further 30−70% reduction) than an equivalent 200 nm spherical nanoparticle. Although a 200 nm spherical nanoparticle provided a reasonable representation of the angular averaged potentials of mean force in Figure 3, it is perhaps unsurprising that it does not provide an accurate model of the translational diffusion coefficient of a confined rod-shaped particle. In this regard, it is worth noting that the dissipative hydrodynamic interactions that influence lateral diffusion have a different physical origin than the conservative electrostatic and van der Waals forces that contribute to the particle−surface interaction potentials.

In the absence of exact theories for the translational diffusion of confined rods, the origin of the decreased MWCNT diffusivity is not obvious. Various combinations of rod dimensions, confinement, hydrodynamic interactions, and electroviscous effects together could all easily slow the MWCNT translational diffusion more than the reference sphere. Although eq 11 is a well-established result for unbounded rod translational diffusion based on rod dimensions, rigorous theories do not exist for the other effects (*i.e.*, limited orientations *via*

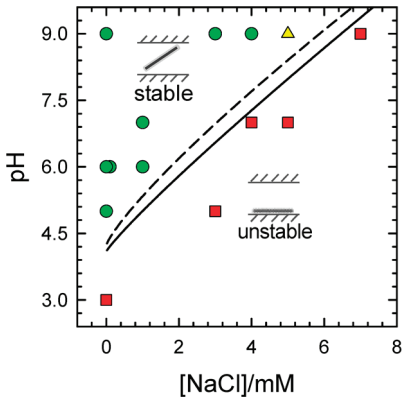

Figure 5. MWCNT stability against deposition on confining SiO_2 walls *vs* [NaCl] and pH. Points indicate cases where >80% of MWCNTs displayed stable potential energy profiles and quasi 2D translational diffusion (green circles), 100% of MWCNTs were irreversibly deposited on SiO_2 substrates (red squares), and ~50% of MWCNT were stable (yellow triangle). Lines indicate predicted stability ratios from eq 12 using the theoretical potentials in Figure 3 (that are in agreement with the measured potentials in Figure 3). The solid line corresponds to $W = 1.5$ (*i.e.*, the rapid deposition limit in the presence of hydrodynamic interactions), and the dashed line corresponds to $W = 100$ (*i.e.*, ~100× slower than the rapid limit; MWCNTs that are stable with respect to deposition on SiO_2).

confinement, hydrodynamic interactions, electroviscous effects). Not being able to predict these other contributions independently makes it difficult to say how these parameters together slow rod diffusion compared to a similar sized spherical nanoparticle. In any case, the measured MWCNT translational diffusivities are of the correct order of magnitude based on their similarity to previous measurements of Au nanoparticles.[14,15] In the future, new theoretical models will be required to understand the differences between confined MWCNT diffusion and the well-understood spherical nanoparticle reference case.[15]

pH and Ionic Strength Dependent Carbon Nanotube Stability and Deposition in Slit Pores. With an understanding of the pH and ionic strength dependent interactions and dynamics of MWCNTs in slit pores, we now measure the stability of MWCNTs and interpret the results in light of the measured interactions and dynamics. Figure 5 shows data indicating whether MWCNTs were stable or unstable against deposition on one of the slit pore walls for different solution chemistries pH = 3−9 and [NaCl] = 0−7 mM. This information was acquired for the same conditions where potentials and diffusion were measured in Figures 3 and 4. These conditions were chosen *a priori* based on characterization showing that the surface potentials vanish at low pH (*e.g.*, Figure 2D) and the general expectation that electrostatically stabilized colloids are not stable above 10 mM ionic strengths (without a steric stabilizer). Stability was determined from EW scattering by measuring many positions within a given batch cell over a period of several hours (from a series of 20 min readings) that showed either (green circles) the majority of MWCNTs experiencing Brownian excursions about the slit pore midplane (*i.e.*, stable), (red squares) all MWCNTs irreversibly deposited (*i.e.*, unstable), or (yellow triangles) the presence of both stable and unstable MWCNTs.

A clear boundary exists between the stable and unstable regions. To understand the pH and ionic strength dependence of this boundary, and further test the potentials directly measured in Figure 3, Figure 5 shows two lines for the stability ratio computed using Fuchs theory eq 12 with hydrodynamic interactions. The Fuchs theory calculation uses the same angular averaged theoretical potentials used to fit the directly measured potentials in Figure 3. The stability ratio is defined as the reciprocal of the actual rate of deposition compared to the rate of rapid deposition. On the basis of this definition, $W = 1$ indicates rapid (*i.e.*, diffusion limited) deposition of MWCNTs in the absence of any repulsive barriers, and $W > 1$ indicates slow (*i.e.*, reaction limited) deposition due to finite energy barriers that result from a sensitive balance of electrostatic repulsion and van der Waals attraction. Hydrodynamic interactions slow aggregation slightly in the rapid limit so that typically $W \approx 1.5$.[21] As a result, Figure 5 shows lines for $W = 1.5$ and $W = 100$ to separate the conditions where particles are expected to rapidly deposit on the slit pore walls and conditions when deposition rates are on the order of 100× slower.

Figure 5 shows that the predicted transition from rapid to slow deposition kinetics coincides with the measured stability boundary, which provides another internal check suggesting the potentials measured in Figure 3 are a reasonable representation of the angular averaged potential of mean force. We include hydrodynamic hindrance in the Fuchs theory calculation based on known results for multibody sphere−wall interactions,[25] although hydrodynamic hindrance plays a minor role that becomes apparent only in the rapid limit. In any case, given the sensitivity of the energy barrier height to the functional form and parameters in the electrostatic and van der Waals attraction potentials, the agreement between the experimental and predicted stability boundaries is impressive within the resolution of the measurements and predictions.

CONCLUSIONS

In conclusion, we have demonstrated a unique capability using EW and VM together to image and measure interactions, diffusion, and stability of individual MWCNTs in model slit pores as a functions of solution and surface chemistry. By approximating the average interaction between MWCNTs as a spherical potential of mean force, we are able to obtain qualitative and quantitative agreement between measured potential energy profiles and deposition behavior.

Although spherical models for hydrodynamic interactions do not accurately capture lateral diffusion of MWCNTs within the slit pores, they show the correct order of magnitude and qualitative trends in agreement with previous measurements of spherical Au nanoparticles. The ability to measure and predict the pH and ionic strength dependent stability boundaries provides a useful tool for understanding how electrostatic and van der Waals interactions determine the transport and stability of MWCNTs in confined geometries. Future work will focus on MWCNTs and slit pore surfaces with different chemistries as well as more accurate measurements and analyses by including more rigorous models of anisotropic rod scattering, interaction potentials, and confined hydrodynamic interactions.

MATERIALS AND METHODS

MWCNTs were purchased from NanoLab Inc. (Waltham, MA), and their surfaces were oxidized using strong acids as previously described.[19] The MWCNTs used in this work exhibited 7.9% surface oxygen as determined by XPS and contained a predominance of carboxylic acid groups. Transmission electron microscopy (TEM) was performed by dipping a holey-carbon TEM grid into a dispersion of MWCNTs and imaging with a Philips CM 300 field-emission gun at 297 kV. Images were collected using a CCD camera mounted on a GIF 200 electron energy loss spectrometer. To prepare stable dispersions, a known mass of MWCNTs was sonicated in 200 mL of deionized water for 20 h. After sonication, the pH was adjusted by adding NaOH or HCl. MWCNT dimensions were measured by atomic force microscopy (Pico SPM LE, Agilent). The bulk translational diffusion coefficients and electrophoretic mobilities were measured using a Malvern Zetasizer (Westborough, MA). Prior to their use in slit pore microscopy measurements, MWCNTs were allowed to sediment for several days. This left only the shortest ones suspended at higher elevations within the vial from which samples were extracted for measurements.

Slit pore cells with MWCNTs dispersed in nanoscale gaps for optical microscopy measurements were prepared in the same way as previous cells used to measure Au nanoparticles.[14,15] In brief, silica spacer particles with a nominal diameter of 320 nm were purchased from Bangs Laboratories, Inc. (Fishers, IN). Glass coverslips (Corning Inc., Corning, NY) were cleaned by soaking in Nochromix (Godax Laboratories, Takoma Park, MD) for 1 h, sonicating in 1 mM KOH for 30 min, rinsing with deionized (DI) water, and drying with nitrogen. Coverslips were assembled into confined cells immediately after cleaning and just prior to experiments. A $\sim$15 μL drop of the MWCNT/spacer colloid mixture (with a large excess of MWCNTs compared to spacers) was placed in the middle of a coverslip (24 $\times$ 50 mm), and then a smaller coverslip (18 $\times$ 18 mm) was suspended on top of the drop *via* surface tension. Excess solution was wicked from the coverslip edges, and the cell was sealed with fast-drying epoxy. The cell was optically coupled with index matching oil to a dovetail prism (see Figure 1A).

Particle trajectories were measured using EW and VM (Axioplan 2, Zeiss, Germany), which is described in detail elsewhere.[16,17,20] A randomly polarized 15 mW, 632.8 nm helium−neon laser (Melles Griot, Carlsbad, CA) was used to generate an evanescent wave decay length of β^{-1} = 113 nm (68° incident angle) at the bottom coverslip/solution interface. A schematic of the experimental setup is shown in Figure 1B. Images were obtained using a 40$\times$ (Achroplan, NA = 0.65) objective (Zeiss, Germany) in conjunction with a 12 bit CCD camera (ORCA-ER, Hamamatsu, Japan) operated at 27 frames/s in 4-binning (336 $\times$ 256 pixels, 204 $\times$ 155 μm^2, 607 nm/pixel). Instantaneous particle heights, z, were obtained *via* their exponential dependence on evanescent wave scattering intensity, $I(z) = I_0 \exp(-\beta z)$.[41,42] Image analysis algorithms coded in FORTRAN were used to track lateral particle coordinates and integrate the evanescent wave scattering intensity for each particle.

Acknowledgment. M.A.B. acknowledges financial support by the National Science Foundation (CTS-0346473, CBET-0834125, CHE-1112335). D.H.F. acknowledges financial support by the National Science Foundation (CBET-0731147, CHE-1112335) and Environmental Protection Agency (RD-83385701-0). We also thank Robert Leheny for useful discussions.

Supporting Information Available: Movies of EW scattering from sub- and superdiffraction limit sized MWCNTs experiencing Brownian motion in a 320 nm slit pore. The superdiffraction limit sized movie shows EW scattering with and without transmitted light. This material is available free of charge *via* the Internet at http://pubs.acs.org.

REFERENCES AND NOTES

1. Javey, A.; Guo, J.; Wang, Q.; Lundstrom, M.; Dai, H. Ballistic Carbon Nanotube Field-Effect Transistors. *Nature* **2003**, *424*, 654–657.
2. Choi, J. H.; Nguyen, F. T.; Barone, P. W.; Heller, D. A.; Moll, A. E.; Patel, D.; Boppart, S. A.; Strano, M. S. Multimodal Biomedical Imaging with Asymmetric Single-Walled Carbon Nanotube/Iron Oxide Nanoparticle Complexes. *Nano Lett.* **2007**, *7*, 861–867.
3. Wiesner, M. R.; Lowry, G. V.; Alvarez, P.; Dionysiou, D.; Biswas, P. Assessing the Risks of Manufactured Nanomaterials. *Environ. Sci. Technol.* **2006**, *40*, 4336–4345.
4. Belin, T.; Epron, F. Characterization Methods of Carbon Nanotubes: A Review. *Mater. Sci. Eng., B* **2005**, *119*, 105–118.
5. Dai, H.; Hafner, J. H.; Rinzler, A. G.; Colbert, D. T.; Smalley, R. E. Nanotubes as Nanoprobes in Scanning Probe Microscopy. *Nature* **1996**, *384*, 147–150.
6. Barber, A. H.; Cohen, S. R.; Wagner, H. D. Measurement of Carbon Nanotube--Polymer Interfacial Strength. *Appl. Phys. Lett.* **2003**, *82*, 4140–4142.
7. Poggi, M. A.; Lillehei, P. T.; Bottomley, L. A. Chemical Force Microscopy on Single-Walled Carbon Nanotube Paper. *Chem. Mater.* **2005**, *17*, 4289–4295.
8. Friddle, R. W.; Lemieux, M. C.; Cicero, G.; Artyukhin, A. B.; Tsukruk, V. V.; Grossman, J. C.; Galli, G.; Noy, A. Single Functional Group Interactions with Individual Carbon Nanotubes. *Nat. Nanotechol.* **2007**, *2*, 692–697.
9. Duggal, R.; Pasquali, M. Dynamics of Individual Single-Walled Carbon Nanotubes in Water by Real-Time Visualization. *Phys. Rev. Lett.* **2006**, *96*, 246104.
10. Tsyboulski, D. A.; Bachilo, S. M.; Kolomeisky, A. B.; Weisman, R. B. Translational and Rotational Dynamics of Individual Single-Walled Carbon Nanotubes in Aqueous Suspension. *ACS Nano* **2008**, *2*, 1770–1776.
11. Fakhri, N.; Tsyboulski, D. A.; Cognet, L.; Weisman, R. B.; Pasquali, M. Diameter-Dependent Bending Dynamics of Single-Walled Carbon Nanotubes in Liquids. *Proc. Natl. Acad. Sci. U. S. A.* **2009**, *106*, 14219–14223.
12. Fakhri, N.; MacKintosh, F. C.; Lounis, B.; Cognet, L.; Pasquali, M. Brownian Motion of Stiff Filaments in a Crowded Environment. *Science* **2010**, *330*, 1804–1807.
13. de Gennes, P. G. Reptation of a Polymer Chain in the Presence of Fixed Obstacles. *J. Chem. Phys.* **1971**, *55*, 572–579.
14. Eichmann, S. L.; Anekal, S. G.; Bevan, M. A. Electrostatically Confined Nanoparticle Interactions and Dynamics. *Langmuir* **2008**, *24*, 714–721.
15. Eichmann, S. L.; Bevan, M. A. Direct Measurements of Protein Stabilized Gold Nanoparticle Interactions. *Langmuir* **2010**, *26*, 14409–14413.

16. Wu, H. J.; Bevan, M. A. Direct Measurement of Single and Ensemble Average Particle-Surface Potential Energy Profiles. *Langmuir* **2005**, *21*, 1244–1254.
17. Wu, H.-J.; Pangburn, T. O.; Beckham, R. E.; Bevan, M. A. Measurement and Interpretation of Particle−Particle and Particle−Wall Interactions in Levitated Colloidal Ensembles. *Langmuir* **2005**, *21*, 9879–9888.
18. Hunter, R. J. *Zeta Potential in Colloid Science: Principles and Applications*; Academic Press: New York, 1981.
19. Smith, B.; Wepasnick, K.; Schrote, K. E.; Cho, H.-H.; Ball, W. P.; Fairbrother, D. H. Influence of Surface Oxides on the Colloidal Stability of Multi-Walled Carbon Nanotubes: A Structure−Property Relationship. *Langmuir* **2009**, *25*, 9767–9776.
20. Bevan, M. A.; Eichmann, S. L. Optical Microscopy Measurements of Kt-Scale Colloidal Interactions. *Curr. Opin. Colloid Interface Sci.* **2011**, *16*, 149–157.
21. Russel, W. B.; Saville, D. A.; Schowalter, W. R. *Colloidal Dispersions*; Cambridge University Press: New York, 1989.
22. Adamczyk, Z.; Warszynski, P. Role of Electrostatic Interactions in Particle Adsorption. *Adv. Colloid Interface Sci.* **1996**, *63*, 41–149.
23. Bevan, M. A.; Prieve, D. C. Direct Measurement of Retarded Van Der Waals Attraction. *Langmuir* **1999**, *15*, 7925–7936.
24. Weinbaum, S. Strong Interaction Theory for Particle Motion through Pores and near Boundaries in Biological Flows at Low Reynold's Number. *Lect. Math. Life Sci.* **1981**, *14*, 119.
25. Pawar, Y.; Anderson, J. L. Hindered Diffusion in Slit Pores: An Analytical Result. *Ind. Eng. Chem. Res.* **1993**, *32*, 743–746.
26. Bevan, M. A.; Prieve, D. C. Hindered Diffusion of Colloidal Particles Very near to a Wall: Revisited. *J. Chem. Phys.* **2000**, *113*, 1228–1236.
27. Tirado, M. M.; Martinez, C. L.; Torre, J. G. d. l. Comparison of Theories for the Translational and Rotational Diffusion Coefficients of Rod-Like Macromolecules. Application to Short DNA Fragments. *J. Chem. Phys.* **1984**, *81*, 2047–2052.
28. Tirado, M. M.; Torre, J. G. d. l. Translational Friction Coefficients of Rigid, Symmetric Top Macromolecules. Application to Circular Cylinders. *J. Chem. Phys.* **1979**, *71*, 2581–2587.
29. Fuchs, N. Uber Der Stabilitat Und Aufladung Der Aerosole. *Z. Phys.* **1934**, *89*, 736–743.
30. Spielman, L. A. Viscous Interactions in Brownian Coagulation. *J. Colloid Interface Sci.* **1970**, *33*, 562.
31. Honig, E. P.; Roebersen, G. J.; Wiersema, P. H. Effect of Hydrodynamic Interaction on the Coagulation Rate of Hydrophobic Colloids. *J. Colloid Interface Sci.* **1971**, *36*, 97–109.
32. Brenner, H. The Slow Motion of a Sphere through a Viscous Fluid Towards a Plane Surface. *Chem. Eng. Sci.* **1961**, *16*, 242–251.
33. Prieve, D. C. Measurement of Colloidal Forces with Tirm. *Adv. Colloid Interface Sci.* **1999**, *82*, 93–125.
34. Lin, M. F.; Shyu, F. L.; Chen, R. B. Optical Properties of Well-Aligned Multiwalled Carbon Nanotube Bundles. *Phys. Rev. B* **2000**, *61*, 14114.
35. Brenner, S. L.; Parsegian, V. A. A Physical Method for Deriving the Electrostatic Interaction between Rod-Like Polyions at All Mutual Angles. *Biophys. J.* **1974**, *14*, 327–334.
36. Hoagland, D. A. Electrostatic Interactions of Rodlike Polyelectrolytes with Repulsive, Charged Surfaces. *Macromolecules* **1990**, *23*, 2781–2789.
37. Parsegian, V. A. *Van Der Waals Forces*; Cambridge University Press: Cambridge, 2005.
38. Lee, H. S.; Yun, C. H.; Kim, H. M.; Lee, C. J. Persistence Length of Multiwalled Carbon Nanotubes with Static Bending. *J. Phys. Chem. C* **2007**, *111*, 18882–18887.
39. Schwarz, S.; Lunkwitz, K.; Kessler, B.; Spiegler, U.; Killmann, E.; Jaeger, W. Adsorption and Stability of Colloidal Silica. *Colloids Surf., A* **2000**, *163*, 17–27.
40. Hunter, R. J. *Foundations of Colloid Science*, 2nd ed.; Oxford University Press: London, 2001.
41. Chew, H.; Wang, D. S.; Kerker, M. Elastic Scattering of Evanescent Electromagnetic Waves. *Appl. Opt.* **1979**, *18*, 2679.
42. Prieve, D. C.; Walz, J. Y. Scattering of an Evanescent Surface Wave by a Microscopic Dielectric Sphere. *Appl. Opt.* **1993**, *32*, 1629–1641.
43. Dagastine, R. R.; Prieve, D. C.; White, L. R. Calculations of Van Der Waals Forces in 2-Dimensionally Anisotropic Materials and Its Application to Carbon Black. *J. Colloid Interface Sci.* **2002**, *249*, 78–83.
44. Hartley, P. A.; Parfitt, G. D. Dispersion of Powders in Liquids. 1. The Contribution of the Van Der Waals Force to the Cohesiveness of Carbon Black Powders. *Langmuir* **1985**, *1*, 651–657.
45. Rajter, R.; French, R. H.; Podgornik, R.; Ching, W. Y.; Parsegian, V. A. Spectral Mixing Formulations for Van Der Waals--London Dispersion Interactions between Multicomponent Carbon Nanotubes. *J. Appl. Phys.* **2008**, *104*, 053513.